High Quality Planar Silicon Nitride Microdisk Resonators for Integrated Photonics in the Visible Wavelength Range

Ehsan Shah Hosseini, Siva Yegnanarayanan, Amir Hossein Atabaki, Mohammad Soltani, and Ali Adibi

School of Electrical and Computer Engineering, Georgia Institute of Technology, 777 Atlantic Drive NW, Atlanta, GA 30332–0250

adibi@ece.gatech.edu

Abstract: High quality factor ($Q \approx 3.4 \times 10^6$) microdisk resonators are demonstrated in a Si_3N_4 on SiO_2 platform at 652–660 nm with integrated in-plane coupling waveguides. Critical coupling to several radial modes is demonstrated using a rib-like structure with a thin Si_3N_4 layer at the air-substrate interface to improve the coupling.

OCIS codes: (130.3120) Integrated optics devices; (230.5750) Resonators.

References and links

1. Y. Akahane, T. Asano, B.-S. Song, and S. Noda, "High-Q photonic nanocavity in a two-dimensional photonic crystal," Nature **425**(6961), 944–947 (2003).
2. E. Kuramochi, M. Notomi, S. Mitsugi, A. Shinya, T. Tanabe, and T. Watanabe, "Ultrahigh-Q photonic crystal nanocavities realized by the local width modulation of a line defect," Appl. Phys. Lett. **88**, 041,112 (2006).
3. T. Barwicz, M. Popović, P. Rakich, M. Watts, H. Haus, E. Ippen, and H. Smith, "Microring-resonator-based add-drop filters in SiN: fabrication and analysis," Opt. Express **12**, 1437–1442 (2004).
4. P. E. Barclay, K. Srinivasan, O. Painter, B. Lev, and H. Mabuchi, "Integration of fiber coupled high-Q SiNx microdisks with atom chips," Appl. Phys. Lett. **89**, 131,108 (2006).
5. D. K. Armani, T. J. Kippenberg, S. M. Spillane, and K. J. Vahala, "Ultra-high-Q toroid microcavity on a chip," Nature **421**, 925–929 (2003).
6. M. Borselli, T. Johnson, and O. Painter, "Beyond the Rayleigh scattering limit in high-Q silicon microdisks: theory and experiment," Opt. Express **13**, 1515–1530 (2005).
7. M. Soltani, S. Yegnanarayanan, and A. Adibi, "Ultra-high Q planar silicon microdisk resonators for chip-scale silicon photonics," Opt. Express **15**, 4694–4704 (2007).
8. C. Manolatou, M. Khan, S. Fan, P. Villeneuve, H. Haus, and J. Joannopoulos, "Coupling of modes analysis of resonant channel add-drop filters," IEEE J. Quantum Electron. **35**, 1322–1331 (1999).
9. D. L. Jeanmarie and R. P. Van Duyne, "Surface Raman Spectroelectrochemistry .1. Heterocyclic, Aromatic, And Aliphatic-Amines Adsorbed On Anodized Silver Electrode," J. Electroanal. Chem. **84**, 1–20 (1977).
10. Z. Lai, Y. Wang, N. Allbritton, G.-P. Li, and M. Bachman, "Label-free biosensor by protein grating coupler on planar optical waveguides," Opt. Lett. **33**, 1735–1737 (2008).
11. J. Campbell, *Introduction to Remote Sensing* (The Guilford Press, 2006).
12. L. Pavesi, L. Dal Negro, C. Mazzoleni, G. Franzò, and F. Priolo, "Optical gain in silicon nanocrystals," Nature **408**, 440–444 (2000).
13. D. Klunder, F. Tan, T. van der Veen, H. Bulthuis, G. Sengo, B. Docter, H. Hokstra, and A. Driessen, "Experimental and numerical study of SiON microresonators with air and polymer cladding," J. Lightwave Technol. **21**, 1099–1110 (2003).
14. N. Ma, C. Li, and A. Poon, "Laterally coupled hexagonal micropillar resonator add-drop filters in silicon nitride," IEEE Photonics Technol. Lett **16**, 2487–2489 (2004).

#112788 - $15.00 USD Received 15 Jun 2009; revised 23 Jul 2009; accepted 23 Jul 2009; published 3 Aug 2009

15. S. Zheng, H. Chen, and A. Poon, "Microring-resonator cross-connect filters in silicon nitride: rib waveguide dimensions dependence," IEEE J. Sel. Top. Quantum Electron. **12**, 1380–1387 (2006).
16. A. Schweinsberg, S. Hocdé, N. Lepeshkin, R. Boyd, C. Chase, and J. Fajardo, "An environmental sensor based on an integrated optical whispering gallery mode disk resonator," Sens. Actuators B. Chemical **123**, 727–732 (2007).
17. K. Ikeda, R. E. Saperstein, N. Alic, and Y. Fainman, "Thermal and Kerr nonlinear properties of plasma-deposited silicon nitride/ silicon dioxide waveguides," Opt. Express **16**, 12,987–12,994 (2008).
18. A. Gondarenko, J. S. Levy, and M. Lipson, "High confinement micron-scale silicon nitride high Q ring resonator," Opt. Express **17**, 11,366–11,370 (2009).
19. E. Krioukov, D. Klunder, A. Driessen, J. Greve, and C. Otto, "Sensor based on an integrated optical microcavity," Opt. Lett. **27**, 512–514 (2002).
20. M. Charlton and G. Parker, "Nanofabrication of advanced waveguide structures incorporating a visible photonic band gap," J. Micromech. Microeng. **8**(2), 172–176 (1998).
21. M. C. Netti, M. D. B. Charlton, G. J. Parker, and J. J. Baumberg, "Visible photonic band gap engineering in silicon nitride waveguides," Appl. Phys. Lett. **76**, 991–993 (2000).
22. J. Baumberg, N. Perney, M. Netti, M. Charlton, M. Zoorob, and G. Parker, "Visible-wavelength super-refraction in photonic crystal superprisms," Appl. Phys. Lett. **85**, 354–356 (2004).
23. M. Charlton, M. Zoorob, M. Netti, N. Perney, G. Parker, P. Ayliffe, and J. Baumberg, "Realisation of ultra-low loss photonic crystal slab waveguide devices," Microelectron. J. **36**, 277–281 (2005).
24. K. Crozier, V. Lousse, O. Kilic, S. Kim, S. Fan, and O. Solgaard, "Air-bridged photonic crystal slabs at visible and near-infrared wavelengths," Phys. Rev. B **73**, 115,126 (2006).
25. M. Barth, J. Kouba, J. Stingl, B. Lchel, and O. Benson, "Modification of visible spontaneous emission with silicon nitride photonic crystal nanocavities," Opt. Express **15**, 17,231–17,240 (2007).
26. E. Krioukov, D. Klunder, A. Driessen, J. Greve, and C. Otto, "Two-photon fluorescence excitation using an integrated optical microcavity: a promising tool for biosensing of natural chromophores," Talanta **65**, 1086–1090 (2005).
27. M. Madou, *Fundamentals of microfabrication: the science of miniaturization* (CRC, 2002).
28. D. Weiss, V. Sandoghdar, J. Hare, V. Lefévre-Seguin, J. Raimond, and S. Haroche, "Splitting of high-Q Mie modes induced by light backscattering in silica microspheres," Opt. Lett. **20**, 1835–1835 (1995).
29. A. Yariv, "Universal relations for coupling of optical power between microresonators and dielectric waveguides," Electron Lett. **36**, 321–322 (2000).
30. A. Yariv and P. Yeh, *Photonics: Optical Electronics in Modern Communications* (Oxford University Press, 2006).
31. H. Haus, *Waves and fields in optoelectronics* (Prentice-Hall, 1984).
32. M. Born and E. Wolf, *Principles of Optics: Electromagnetic Theory of Propagation* (Cambridge University Press, 1999).
33. M. Soltani, S. Yegnanarayanan, Q. Li, and A. Adibi, "Systematic Engineering of Waveguide-Resonator Coupling for Silicon Microring/Microdisk/Racetrack Resonators: Theory and Experiment," submitted (2008).
34. M. Soltani, Q. Li, S. Yegnanarayanan, and A. Adibi, "Improvement of thermal properties of ultra-high Q silicon microdisk resonators," Opt. Express **15**, 17,305–17,312 (2007).
35. S. Chuang, "A coupled mode formulation by reciprocity and a variational principle," J. Lightwave Technol. **5**, 5–15 (1987).

1. Introduction

Optical resonators, with the capability of trapping and storing photons for long periods of time, are essential parts of the optical integrated systems. Two common structures, used extensively in today's integrated circuits, are photonic crystal cavities [1, 2], and traveling wave resonators (microrings [3], microdisks [4], and microtoroids [5]). Realization of whispering gallery mode (WGM) resonators in silicon-based material systems has great benefits, such as ease of fabrication, integrability with mature silicon (Si) electronics, and low cost. These novel structures have already been demonstrated on silicon oxide (SiO_2) [5], silicon [6], and silicon nitride (Si_3N_4) materials [4]. While SiO_2 micro-toroid and micro-sphere resonators have shown the highest Q's [5], their size and lack of chip-scale integrability (because of the bulky fiber taper coupling scheme) result in complications in using them for integrated photonics applications. On the other hand, Si microdisks on oxide substrates have recently been shown to be capable of achieving high quality factors ($Q > 10^6$) while being coupled to planar optical waveguides [7]. [8]

We believe that integrated nanophotonics in the visible range of the spectrum could serve

#112788 - $15.00 USD Received 15 Jun 2009; revised 23 Jul 2009; accepted 23 Jul 2009; published 3 Aug 2009

as a new platform for sensing and optical data processing applications. Photonic structures that guide and manipulate light in the visible spectral range are not as well investigated as their IR counterparts. Nevertheless, this spectral range is important for applications such as biological sensing (e.g., using fluorescence and surface enhanced Raman spectroscopy (SERS) [9, 10]), and visible wavelength reconfigurable optical signal processing (for applications such as LiDAR [11]). By adding light generation and detection in the visible range (using Si [12]) to the Si_3N_4 photonic device on the same substrate, it is possible to develop all visible nanophotonic components, including sources, modulators, waveguide components, and detectors on a monolithic CMOS-compatible photonic chips; thereby forming complete system-on-chip solutions.

Despite their good performance in the infrared (IR) region, Si resonators suffer from significant material loss in the visible range of the optical spectrum, making them unsuitable for visible light applications. Unlike silicon, low Si content, LPCVD Si_3N_4 offers a very low material loss throughout the optical range (wavelengths from 300 nm to several microns), and a moderately high refractive index ($n \approx 2$). Si_3N_4, being a dielectric material, does not suffer from free carrier absorption, which is an important limiting factor in Si high-Q resonators. This makes the fabrication process more straightforward by eliminating the complicated surface treatment post processes necessary for high-Q silicon resonators [6]. On the other hand, having the absorption band edge located at approximately 300 nm wavelength, two photon absorption is not a limiting factor at high intensities at wavelengths larger than 600 nm. Thus, provided that the Si_3N_4 layer is optically isolated from the lossy Si substrate, it can guide the visible light without significant loss in this wavelength range. Nevertheless, most of the research on silicon nitride has been concentrated on infrared (IR) [13, 14, 15, 16, 17, 18] or near infrared (NIR) [19, 4] applications. The few reported works on Si_3N_4 photonic crystals [20, 21, 22, 23, 24, 25] and microring resonators [26] in the visible range were of considerably lower fabrication quality compared with their Si counterparts.

In this work, monolithic, high Q, compact Si_3N_4/SiO_2 resonators are demonstrated in the visible range, and critical coupling of the resonators to in-plane waveguides is also demonstrated (at λ=652-660 nm). Details of fabrication of the devices are explained in section 2. The characterization setup and the experimental results are discussed in section 3. Coupling of high Q resonators to adjacent waveguides and its optimization are covered in section 4. Final conclusions are made in section 5.

2. Fabrication

Fabrication of these structures is done on top of a thermally grown, 6-micron-thick oxide layer, which isolates the guiding Si_3N_4 layer from the lossy Si substrate (as shown in Fig. 1(a)). A 200 ± 3 nm-thick layer of low loss, stoichiometric Si_3N_4 is then deposited on top of the oxide using low pressure chemical vapor deposition (LPCVD). The LPCVD deposition was done at the LioniX foundry. The resulting films were slightly higher in Si content and the refractive index of the silicon nitride layer, without any subsequent annealing, was almost %1 higher than the nitride films reported elsewhere [27]. For fabrication of the microresonators, 500 nm of ZEP-520 electron beam resist is used as the etching mask. In order to inhibit the surface charge-up during the electron beam writing, a thin layer of Espacer 300 is spun on top of the resist. The waveguides and microdisks with the desired coupling gap between them are patterned using a JEOL JBX-9300FS 100kV electron beam lithography system. The pattern addressing grid size is 1 nm, the beam scanning frequency is f=50 MHz, and the beam current is set to I=2 nA (using 60 μm aperture). Choosing a dosage of D=250 $\mu C/cm^2$ for the ZEP, the smallest possible shot pitch (SP) is 4 nm ($SP \geq [I/(f \cdot D)]^{1/2}$). Moreover, the beam spot size for the 2 nA current is approximately 6 nm. We expect that with such shot pitch and beam spot size,

#112788 - $15.00 USD Received 15 Jun 2009; revised 23 Jul 2009; accepted 23 Jul 2009; published 3 Aug 2009

the roughness introduced to the structure during the electron beam lithography is smaller than 10 nm (Fig. 1(c)). The etching is then performed using CF_4 gas in an STS inductively coupled plasma (ICP) etcher, in which a detailed optimization of the etching process is performed to minimize the sidewall roughness and thus to maximize the *Q*. The optimized pressure, coil power, and platen power are P=5 mTorr, P_c=600 W, and P_p=20 W, respectively. The sidewall roughness is inspected with scanning electron microscopy (SEM), and the sidewall tilt angle is measured to be 85°. A scanning electron microscopy (SEM) image of a microdisk resonator coupled to a waveguide is shown in Fig. 1(b) and the smoothness of the etched sidewalls is apparent from Fig. 1(c).

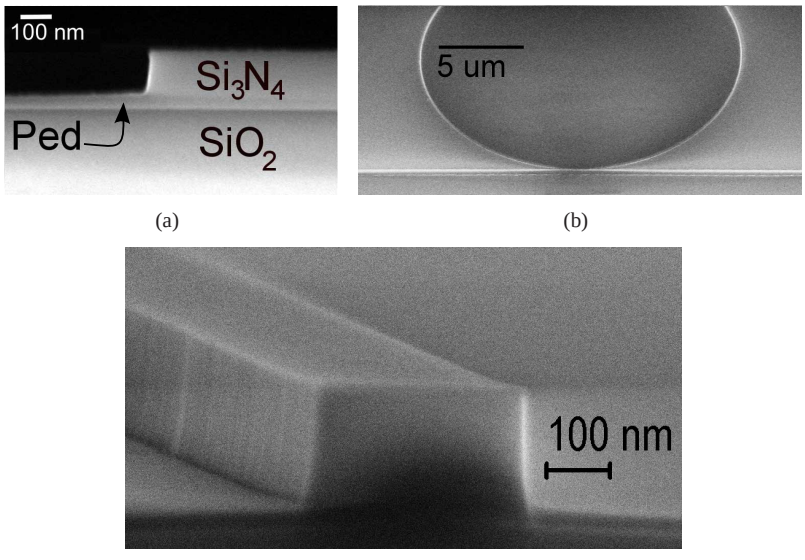

(a) (b)

(c)

Fig. 1. (a) SEM image of a waveguide etched on a 203 nm layer of Si_3N_4 on top of 6 μm of isolating SiO_2 on a Si substrate. A Si_3N_4 pedestal layer is created to enhance the in-plane coupling strength of the resonators to the waveguides to achieve critical coupling. This layer is accurately defined during the etching by controlling the etch time of the ICP plasma process. (b) Tilted SEM image of a microdisk resonator side-coupled to an in-plane single mode waveguide with a 190 nm coupling gap. The radius of the disk is 20 μm. (c) The cleaved facet of a low roughness a waveguide etched using the optimized plasma etching parameters.

3. Characterizations

To characterize the fabricated structures, the output light of a tunable laser diode source (New Focus™TLB-6305) is coupled to the cleaved facet of the waveguide using a microscope objective lens. The wavelength of the laser is swept across the 652–660 nm wavelength range in 0.25 pm steps, and the transmission is measured as a function of wavelength by a Si detector at the waveguide output. The polarization of interest in this work is TE (transverse electric i.e., electric field in the plane of the resonator). Figure 2(a) shows the transmission spectrum for the structure shown in Fig. 1(a). Each dip in Fig. 2(a) corresponds to a TE cavity mode.

While the resonator has several modes, we have limited our characterization bandwidth to the range of 652–660 nm that is available from the characterization laser. Each $TE_{p,m}$ is characterized by its radial order (*p*) and azimuthal order (*m*). The dips in the transmission spectrum in Fig. 2(a) are attributed to different modes using the detailed theoretical analysis

#112788 - $15.00 USD Received 15 Jun 2009; revised 23 Jul 2009; accepted 23 Jul 2009; published 3 Aug 2009

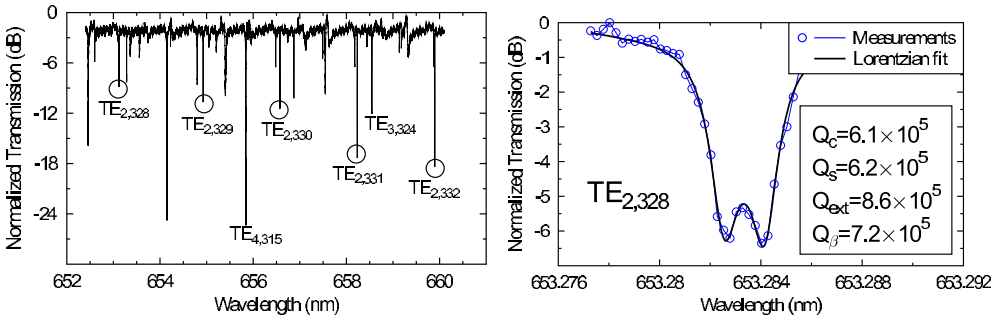

(a) (b)

Fig. 2. (a) The normalized transmission of the waveguide coupled to the microdisk shown in Fig. 1(b). Each dip in the spectrum represents a specific $TE_{p,m}$ resonance in which p and m are respectively the number of radial and azimuthal antinodes. The dips denoted by the circles are due to $TE_{2,m}$ family of modes, which have the highest quality factor among all the radial families (for a 20 μm radius disk). The mode identification is based on the free spectral range (FSR) of the modes, matched with the FEM simulation data in Table 1. (b) Transmission spectrum zoomed around $TE_{2,328}$. By fitting a double-Lorentzian lineshape to the experimental data, the intrinsic Q of $TE_{2,328}$ is found to be about 6.1×10^5.

of the resonator mode structure using the finite element method (FEM) implemented in the COMSOL® environment. Variant transmission levels at different radial modes are due to unequal coupling levels to the adjacent waveguide. The full width at half maximum (FWHM) of each dip $(\Delta\lambda)$ can be used to measure the loaded Q of that mode using $Q=\lambda_o/\Delta\lambda$, with λ_o being the central resonance wavelength of the mode in air. Figure 2(b) shows the zoomed version of the $TE_{2,328}$ resonance mode in Fig. 2(a) for which an intrinsic $Q_o = 6.1\times10^5$ is measured. As seen in Fig. 2(b), the back-scattering from the sidewall roughness results in coupling of the clockwise (CW) and counterclockwise (CCW) modes, leading to a doublet mode splitting [28]. Thus, the extraction of the Q from the experimental results is done by fitting a double-Lorentzian line shape with Q_c, Q_s, Q_{ext}, and Q_β as the fit parameters [6]. Q_c and Q_s represent the intrinsic quality factors of the two microdisk standing wave modes, while Q_{ext} and Q_β show the loading and back-scattering coupling Q's, respectively. The important properties of the first four radial order modes of the microdisk resonator in Fig. 1(b) (with 20 μm radius and a pedestal thickness of 50 nm) are summarized in Table 1. The results in table 1 are calculated using the FEM simulations.

Table 1. *Measured* intrinsic quality factor (Q_o), *simulated* normalized mode volume ($V(n/\lambda_o)^3$), *simulated* effective index of the disk defined as $n_{disk}\equiv m/(k_oR)$, and the free spectral range (FSR) of the first four radial TE modes of the Si_3N_4 microdisk with $R=20$ μm, thickness of $d=203$ nm and a pedestal layer of $ped=50$ nm (k_o is the free–space wavenumber $k_o\equiv 2\pi/\lambda_o$). TE_2 mode has the highest quality, and TE_1 has the smallest mode volume.

	Q	$V^\dagger$	$(Q/V)^\ddagger$	n_{disk}	FSR
TE_1	5.10×10^5	352	1449	1.78	1.64 nm
TE_2	6.10×10^5	470	1297	1.73	1.66 nm
TE_3	2.00×10^5	515	388	1.68	1.68 nm
TE_4	1.10×10^5	670	178	1.65	1.69 nm

†,‡ The mode volume is normalized to $(\lambda/n)^3$.

By increasing the microdisk radius, the scattering of the resonance mode to the radiation

#112788 - $15.00 USD Received 15 Jun 2009; revised 23 Jul 2009; accepted 23 Jul 2009; published 3 Aug 2009

modes due to fabrication imperfections is reduced. And therefore, higher values of Q can be obtained. To verify this, we fabricated and characterized microdisks with a radius of 100 μm (the height of the Si_3N_4 layer, the pedestal height, the coupling gap, and the waveguide width are the same as those of the structure in Fig. 1(b)). Figure 3(a) shows the transmission spectrum of this larger disk. The comparatively large size of the disk leads to larger number of nonleaky modes and also to a smaller FSR for each radial order mode. Therefore, the spectrum in Fig. 3(a) is much more condensed with the resonant dips in transmission than that in Fig. 2(a). Figure 3(b) shows the spectrum of one of the resonant modes of the 100 μm radius microdisk for which a $Q_o \approx 3.4 \times 10^6$ was measured.

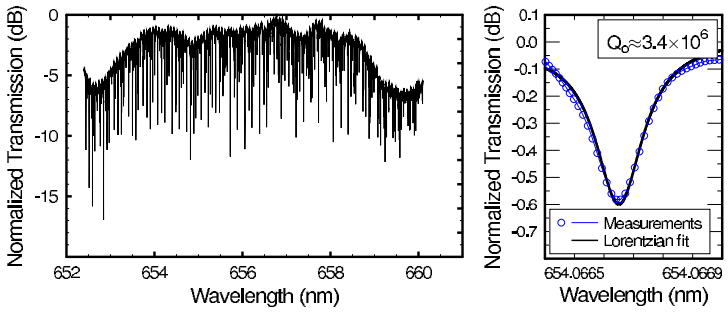

(a) (b)

Fig. 3. (a) The normalized transmission of a waveguide coupled to a large microdisk with radius $R = 100$ μm (other properties of the structure are the same as those in the caption of Fig. 2(b). (b) Transmission spectrum zoomed around one of the high Q resonant modes of the $R = 100$ μm microdisk resonator in (a). The intrinsic quality factor of the higher Q mode is $Q_o = 3.4 \times 10^6$.

4. Coupling

Most applications of high Q resonators (e.g., sensing, nonlinear optics, and quantum optics) require high field intensity inside the resonator. This requires very good coupling between the resonator and the adjacent waveguide or fiber. The maximum coupling between a waveguide and a cavity can be close to 100% when the rate of energy coupling from the waveguide to the cavity is equal to the rate of energy loss in the cavity [29]. The transmission function for the coupled structure in Fig. 1(a) is

$$T(\omega_o) = \frac{P_{out}(\omega_o)}{P_{in}(\omega_o)} = \left| \frac{Q_o - Q_c}{Q_o + Q_c} \right|^2 \tag{1}$$

where Q_o and Q_c are respectively the intrinsic Q and the coupling Q and $P_{in}(\omega_o)$ and $P_{out}(\omega_o)$ are the input and output power in the waveguide before and after coupling to the resonator, respectively. When $Q_o = Q_c$ the transmission function of the waveguide becomes zero at the resonance frequency and the waveguide mode energy is completely transferred to the microresonator. This special situation, called critical coupling [30], can be achieved by optimizing the gap between the waveguide and the cavity in Fig. 1(b). We perform this optimization by detailed analysis of the structure in Fig. 1(b) for different waveguide-cavity gaps using coupled-mode theory [31] implemented in the COMSOL® finite element method (FEM) package [7]. To accurately model the resonator in Fig. 1(b), the index of the Si_3N_4 film is measured using ellipsometry and fitted to a Cauchy model [32] ($n \approx 2.07$ at 655 nm). Here, just the first few radial mode orders of the disk are of concern as the less confined higher-order modes have lower effective mode indices and eventually become leaky. For example, in a 20

#112788 - $15.00 USD Received 15 Jun 2009; revised 23 Jul 2009; accepted 23 Jul 2009; published 3 Aug 2009

μm radius disk, only the first eight TE and the first four transverse magnetic (TM) modes are well-confined inside the resonator. Here, we will concentrate on the TE modes; the results from the TM modes are comparable, nonetheless. As an example, Fig. 5 shows the magnetic field pattern for the first TE mode of the Si_3N_4 pedestal resonator with radius $R=20$ μm and the adjacent waveguide with 380 nm width at a distance (gap) of g=190 nm. The thickness of the Si_3N_4 pedestal layer is 50 nm. The coupling strength between the waveguide and the cavity depends on the field overlap as well as phase mismatch of the two structures.

Using the coupled mode theory, it can be shown that to get significant coupling from the waveguide to the microdisk resonator, the coupling rate should be close to the intrinsic loss of the resonator [30]. Our calculations show that for a 20 μm radius disk with $Q < 1\times10^6$, the coupling gap should be narrower than 100 nm for critical coupling to the first few modes, which renders the fabrication of such structures challenging and non-repeatable with current electron beam lithography and ICP etching tools. This is primarily due to the insufficient overlap of the waveguide field with the first few more confined (and hence higher Q_o) TE modes at large gaps. To solve this issue, we add a thin (50 nm) pedestal Si_3N_4 layer—fabricated by proper selection of the etching time of the pedestal region—around the microdisk as shown in Fig. 5. The addition of the pedestal layer results in stronger field overlap between the waveguide and the resonator, thereby enabling critical coupling to the low-order higher Q modes at gap distances larger than 200 nm (more detail can be found in Ref. [33]). In addition to facilitating the critical coupling to the high Q mode, the added pedestal layer improves the thermal and mechanical properties of the microdisk cavity [34].

The coupling coefficient between a waveguide and an adjacent cavity is given by the first order perturbation theory [35, 8], and can be written as

$$\kappa = \frac{i\omega\varepsilon_o}{4}\int_{-\infty}^{\infty}\int_{0}^{W}\int_{ped}^{d}(n_{SiN}^2-1)\,\mathbf{E}_{\text{disk}}\cdot\mathbf{E}_{\text{wg}}e^{j\phi}\,\mathrm{d}y\,\mathrm{d}x\,\mathrm{d}z \tag{2}$$

in which $\mathbf{E}_{\text{disk}}$ and $\mathbf{E}_{\text{wg}}$ correspond to the amplitude of the electric fields of the disk and the waveguide, respectively; n_{SiN} is the bulk index of the Si_3N_4. The phase factor ϕ is the difference between the propagation phases of the waveguide and the cavity mode, and it can be approximated as

$$\begin{aligned}
\phi = \phi_{disk}-\phi_{wg} &= -m\theta+\beta_{wg}z && \text{(z is the direction of waveguide propagation)}\\
&\approx -m(z/(R+g+W/2))+\beta_{wg}z && \text{(for small z, } \theta\approx z/(R+g+W/2))\\
&= -n_{disk}k_o zR/(R+g+W/2)+n_{wg}k_o z && \text{(at resonance, } 2\pi Rn_{disk}k_o=2\pi m)\\
&= k_o z(n_{wg}-n_{disk}\xi). && \text{(we define } \xi\equiv\tfrac{R}{R+g+W/2})
\end{aligned} \tag{3}$$

In this formulation, $k_o=2\pi/\lambda_o$ is the wavenumber in free space, β_{wg} is the propagation constant of the waveguide mode, m is the azimuthal mode order of the resonator, g is the gap between the microdisk and waveguide, W is the waveguide width, R is the resonator radius and $\xi\equiv R/(R+g+W/2)$ is defined for brevity (more detail can be found in [33]). The effective index of the disk and the waveguide is defined as $n_{disk}\equiv m/k_oR$ and $n_{wg}\equiv\beta_{wg}/k_o$, respectively. It is clear form Eq. (2) that the phase mismatch $k_oz(n_{wg}-n_{disk}\xi)$ between the two structures can reduce the coupling coefficient considerably. Since we are in the regime of small overlap between the resonator and waveguide fields, it is essential to achieve close to complete phase matching to allow for critical coupling with a reasonably large gap between waveguide and the cavity. This happens approximately when n_{wg}/ξ and n_{disk} are equal [7].

The simulated effective index of the TE mode of the waveguide, multiplied by $1/\xi$ is plotted in Fig. 6(a) as a function of W in the range that the waveguide supports only one mode in the TE

#112788 - $15.00 USD Received 15 Jun 2009; revised 23 Jul 2009; accepted 23 Jul 2009; published 3 Aug 2009

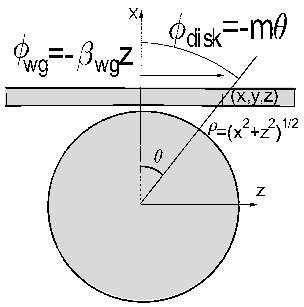

Fig. 4. Digram of a disk side-coupled to a waveguide. The phase of $\mathbf{E}_{\text{disk}}$ at any point can be evaluated as $\phi_{disk} = -m\theta$ in which θ is calculated in reference to the $z = 0$ plane. The waveguide field ($\mathbf{E}_{\text{wg}}$), on the other hand, experiences a linear phase change along the waveguide $\phi_{wg} = -\beta_{wg}z$.

polarization W =150–550 nm with the other properties of the waveguide are kept at $h = 200$ nm and $ped = 50$). The horizontal lines in 6(a) depict the effective indices (n_{disk}) of the first four TE modes (with the lower order modes having higher effective indices). The approximate optimal waveguide width for coupling to each resonator mode can be deduced from the crossing points. Nevertheless, it is noteworthy that, as the distance between the waveguide and the resonators increases rapidly with propagation along the z direction, the above argument provides just an *approximation* for waveguide width that provides the maximum coupling. Therefore, for a better determination of the optimal waveguide width (W), a rigorous calculation of Eq. (2) is required [33]. Therefore, for a better determination of the optimal coupling width, a rigorous calculation of Eq. (2) is required [33]. We performed this calculation using $TE_{2,m}$–$TE_{4,m}$ to obtain the field distribution of the microdisk and waveguide modes and calculating the coupling quality factor (Q_c) as a function of the waveguide width for the waveguide–cavity coupled structure shown in Fig. 5. The minimum of each curve in Fig. 6(b) corresponds to the highest level of coupling between the waveguide and each cavity mode. The waveguide width (W) for each minimum in Fig. 6(b) is approximately equal to the corresponding crossing points in Fig. 6(a). This shows the reasonable accuracy of the approximate index model used in the derivation of the results in Fig. 6(a). Note that the critical coupling is achieved when $Q_c = Q_o$ and this does not necessarily correspond to the minimum of the Q_c–W curve and can even be satisfied at two different waveguide widths.

As the width of the fabricated waveguide is 380 nm, the expected coupling Q to $TE_{1,m}$ from Fig. 6(b) is much larger than the other three higher order modes ($TE_{2,m}$–$TE_{4,m}$)(see 6(b)).

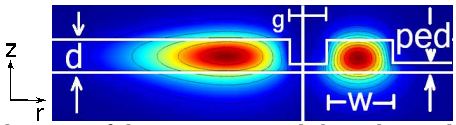

Fig. 5. (left) H_z field pattern of the $TE_{2,328}$ microdisk mode simulated with COMSOL® using a cylindrical symmetry. (right) The vertical magnetic field (H_z) of the first-order mode is demonstrated. The two-dimensional cross section of the single mode waveguide is also simulated and the coupling between them is estimated. A pedestal layer, which is achieved with partial etching of the silicon nitride layer, is used to increase the coupling coefficient. W, d, ped, and g denote the waveguide width, Si_3N_4 layer thickness, the pedestal height, and the gap between the waveguide and the cavity, respectively. In the field simulated, d=200 nm, W=380 nm, and ped=50 nm.

#112788 - $15.00 USD Received 15 Jun 2009; revised 23 Jul 2009; accepted 23 Jul 2009; published 3 Aug 2009

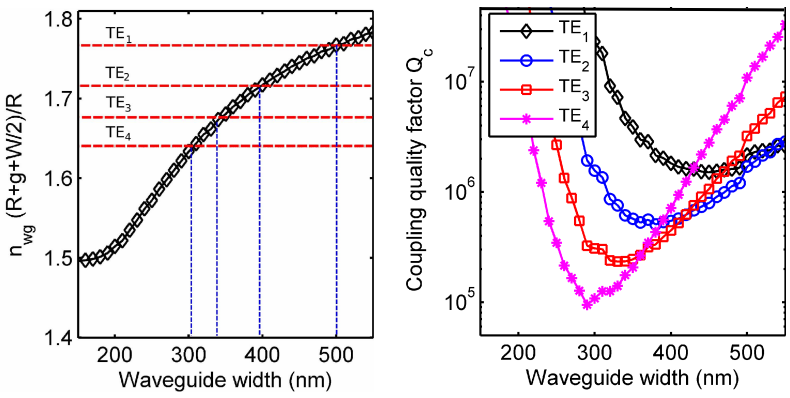

Fig. 6. (a) The effective index of the TE mode of the waveguide multiplied by $1/\xi = (R+g+W/2)/R$ as a function of the waveguide thickness (W) with $h = 200$ nm and $ped = 50$ nm . The horizontal lines depict the effective indeces of the different TE radial mode orders, with the first mode (TE_1), having the highest effective index. (b) The coupling quality factor (Q_c) as the function of the waveguide width with a constant gap of 190 nm and the other parameters as mentioned in the caption of Fig. 5.

Comparing the intrinsic quality factors listed in Table 1 with the calculated coupling Q from Fig. 6(b), it is expected not to observe significant coupling to the $TE_{1,m}$ compared with the coupling to $TE_{2,m}$–$TE_{4,m}$ modes. This agrees with the measurement results (shown in Fig. 2(a)). On the other hand, identification of the dips in Fig. 2(a) is consistent with this, as the larger dips in transmission are due to $TE_{2,m}$–$TE_{4,m}$ modes. Note that in our analysis in this paper, we fixed a few parameters in the coupled structure to investigate the effect of a specific design parameter. In general, the thickness of the pedestal layer, the gap between the waveguide and the resonator, and the widths of the waveguide are the parameters to be optimized for coupling to the desired high Q modes of a microdisk resonator with the specific radius.

5. Conclusion

We presented here a detailed investigation of the properties of Si_3N_4 microdisk resonators on substrate at visible wavelengths. We showed that it is possible to fabricate these resonators with high quality factors and small mode volumes. The ultra-high Q_o of 3.4×10^6 for a 100 μm radius microdisk is, to the best of our knowledge, the largest reported to date for a microdisk structure at visible wavelength (652–660 nm in our case). We also showed the possibility of achieving critical coupling between a desired cavity mode and an adjacent waveguide through the engineering of the gap between the waveguide and the cavity and adding a thin ($\approx$50 nm) pedestal layer [33]. Since the existing quality factors of 20 μm radius microdisks are not limited by the material loss, we expect to be able to considerably improve them by further optimization of the resonator structure and improvement in the fabrication process.

Acknowledgments

This work was supported by the air force office of scientific research (AFOSR) through Dr. G. Pomrenke under contract No. FA9550–06–01–2003

#112788 - $15.00 USD Received 15 Jun 2009; revised 23 Jul 2009; accepted 23 Jul 2009; published 3 Aug 2009